

SUPPLEMENTAL MATERIAL for

Detrital glass in a Bering Sea sediment core yields a ~160 ka middle Marine Isotope Stage 6 age for Old Crow tephra

Alberto V. Reyes, Britta J. L. Jensen, Shaun Woudstra, Matthew S.M. Bolton, Serhiy D. Buryak, Mea S. Cook, Jordan Harvey, John A. Westgate

1.1 Site U1345 age-depth model and isotope stratigraphy

Cook et al. (2016) generated the age-depth model for the primary core splice at Site U1345. Briefly, a multi-species assemblage of benthic foraminifera was picked from from the >150 μm size fraction of core sub-samples and analyzed for $\delta^{18}\text{O}$ by standard methods. Marine Isotope Stages in U1345 were identified by selecting depths at the mid-point of transitions between glacial and interglacial intervals in the $\delta^{18}\text{O}$ record and tuning those depths to the glacial/interglacial boundaries in the LR04 global benthic $\delta^{18}\text{O}$ stack (Lisiecki and Raymo, 2005).

Cook et al. (2016) provide estimates for uncertainty in identifying the depth for certain MIS boundaries in the primary core splice (Table 2 of Cook et al., 2016). Deglaciation timing for Termination II was not well constrained in the Cook et al. (2016) age model for Site U1345 due to poor carbonate preservation and low benthic foraminifera abundance. We refined the U1345 age model during the time periods of the purported ages of the Old Crow tephra. We added an additional well-defined age control point at the $\delta^{18}\text{O}$ maximum during MIS 7 (Table S1; Fig. S1). We also increased the precision of the depth for the MIS 6-5 boundary using bulk sediment $\delta^{15}\text{N}$ to tie U1345 to nearby Site U1343 (main text Fig. 1), which has good carbonate preservation and a highly resolved benthic $\delta^{18}\text{O}$ record for the MIS 6-5 transition (Asahi et al., 2016; Worne et al., 2019). Unpublished bulk sediment $\delta^{15}\text{N}$ for Site U1345 (Mea Cook, unpublished data; Fig. S1) was measured on a Carlo Erba 1108 elemental analyzer coupled to a Thermo-Finnigan Delta Plus XP isotope ratio mass spectrometer (EA-IRMS) at the University of California, Santa Cruz, following [Knudson and Ravelo \(2015\)](#). An abrupt $\delta^{15}\text{N}$ decrease in U1343 is coincident with the benthic $\delta^{18}\text{O}$ decrease of the penultimate deglaciation (Worne et al., 2019; Fig. S1). Sites U1343 and U1345 are expected to have similar $\delta^{15}\text{N}$ through time because they are both located on the continental slope in the Bering Sea "Green Belt" (Springer et al., 1996) and have similar nutrient utilization and productivity today. Therefore, we assumed that the midpoint of the $\delta^{15}\text{N}$ decrease in U1345 was also the midpoint of the deglacial transition, which allowed us to increase the precision estimate for the depth of the MIS 6-5 transition. Compared to the published Cook et al. (2016) age model, this revised age model yields ages for sampled depths in this study that are ~3 kyr younger for MIS 5, ~1.5–2.5 kyr younger for MIS 6, and ~2.5–7 kyr older for MIS 7. The interpretations in the main text are not affected by these minor age model revisions.

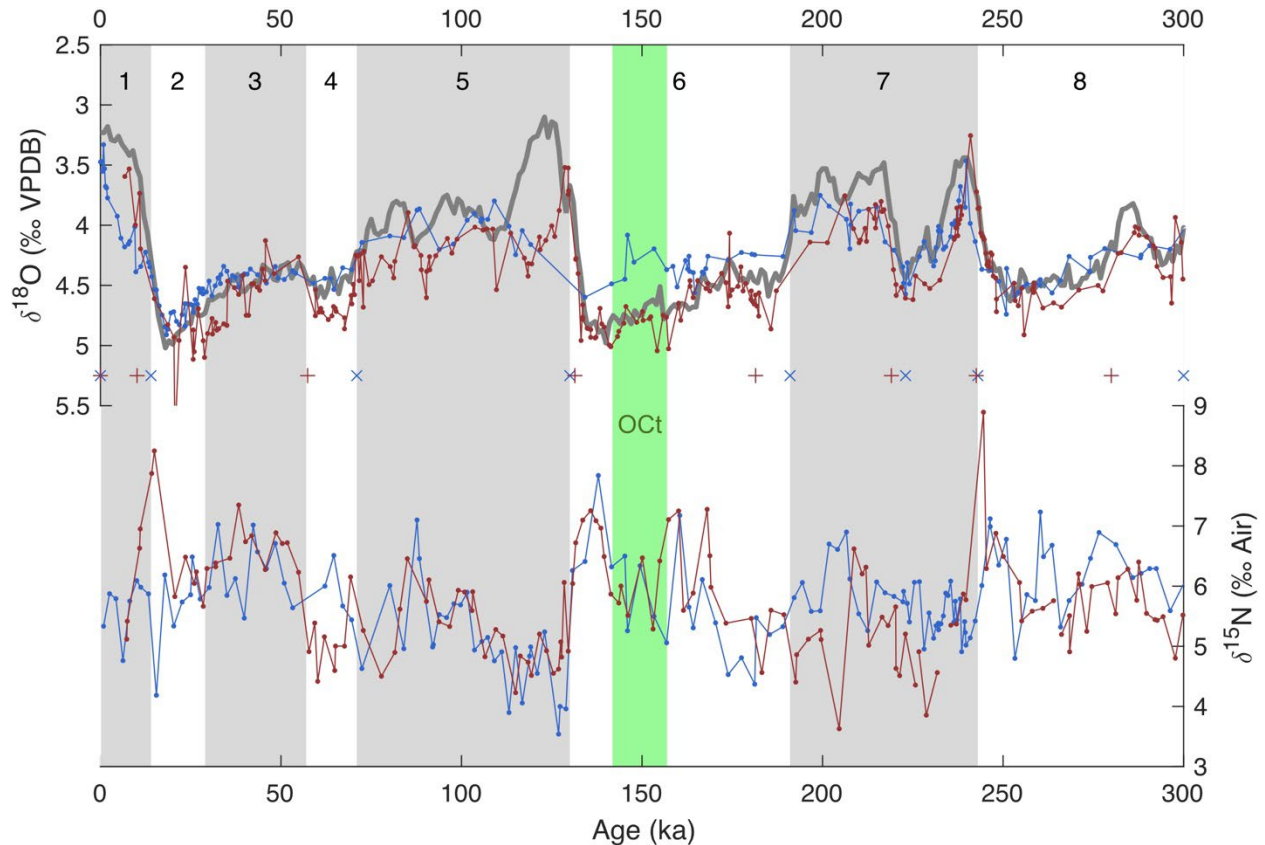


Fig. S1: Top: The benthic foraminiferal $\delta^{18}\text{O}$ in U1345 (blue; Cook et al., 2016) and U1343 (red; Worne et al., 2019) with the LR04 global benthic $\delta^{18}\text{O}$ stack (grey; Lisiecki and Raymo, 2005). The U1345 data are on the updated age model (this study). The multi-species U1343 and U1345 data have been corrected to *U. peregrina* (offsets in Cook et al., 2016; Asahi et al., 2016). Tie points to LR04 for the U1345 and U1343 age models are indicated with "+" for U1343 and "x" for U1345. Bottom: The bulk $\delta^{15}\text{N}$ from U1345 (Mea Cook, unpublished data) and U1343 (Worne et al., 2019). Vertical green bar marks the ~15 kyr interval of Site U1345 with ~40-60% concentration of detrital Old Crow tephra shards.

We estimated age uncertainty for our sampled intervals at Site U1345 by: (1) calculating sedimentation rates between tie points from the updated age model, with the sedimentation rates at each age control point calculated as the average of the overlying and underlying sedimentation rate; (2) converting the age control point depth uncertainty to age uncertainty using the calculated sedimentation rate at that tie point; (3) combining in quadrature the age uncertainty for U1345 tie points with the estimated 4 kyr age uncertainty (2σ) for glacial-interglacial transitions in the LR04 benthic stack; (4) Bayesian age-depth modeling using the BACON package (Blaauw and Christen, 2011) in R (R Core Team, 2022), defined by the age uncertainties for tie points calculated in (3), and with boundaries defined for the age control points and accumulation rate priors between boundaries as the calculated sedimentation rates.

The 2σ age model uncertainties from BACON are ~4–9 kyr, with the highest uncertainty during MIS 6 between ~142 and 181 ka (Table S2). Uncertainty in the age-depth model does not affect the identification of glacial and interglacial stages. The $\delta^{18}\text{O}$ double-minima during MIS 7 are clearly identified, as is the sustained interval of high $\delta^{18}\text{O}$ during MIS 6 (Fig. S1, top). The abrupt $\delta^{18}\text{O}$ drop during the MIS 6-5 transition is clearly identified in U1343 (Fig. S1, top), and abrupt decreases in $\delta^{15}\text{N}$ correlate U1345 to U1343 during that deglacial interval. Old Crow tephra appears abruptly 157 ± 9 ka, shortly before the MIS 6 glacial maximum indicated by maxima in benthic $\delta^{18}\text{O}$ (main text Fig. 2) and bulk $\delta^{15}\text{N}$ (Fig. S1), and persists at high concentration for ~15 kyr until $\sim 142 \pm 8$ ka (Fig. S1; main text Fig. 2).

1.2 Detrital tephra preparation and analysis

Glass shards were separated from archived 2-cm half-round samples taken from cores that make up the IODP Site U1345 primary splice. The archived samples had been freeze-dried, sieved to isolate the 63–150 μm size fraction, then oven-dried (Cook et al., 2016). Details on sedimentology and bioturbation of sampled depth intervals from the various cores that make up the primary splice from Site U1345 are given in Table S2.

Glass shards were first separated from the heavy mineral fraction using lithium heteropolytungstate (LST) heavy liquid at 2.45 g cm^{-3} , followed by a second separation at 2.10 g cm^{-3} for samples with abundant biogenic silica. Glass shards were mounted on pucks in epoxy, polished, and carbon-coated for analysis by electron probe microanalysis (EPMA) on a JEOL JXA-8900R at the University of Alberta.

Instrument calibration was by mineral and glass standards. We determined major-element composition of glass shards by wavelength-dispersive spectrometry, with a 10 μm defocused beam, 15 keV accelerating voltage, and 6 nA beam current. These instrument conditions minimize potential for Na and K migration during analysis of glass. We bracketed analysis of unknowns (every ~75 shards) with two matrix-matched standards of known composition: ID3506 (the rhyolitic Lipari obsidian) and a reference sample of the secondarily hydrated rhyolitic Old Crow tephra, both of which are commonly used as secondary standards for glass analyses (Kuehn et al., 2011).

All data were normalized to 100 wt% on a water-free basis. Final data were screened for data quality, and analyses subject to clear contamination by microlites or epoxy were removed from further consideration. The vetted detrital tephra dataset is provided as an Excel file in Data Set 1. Full results for secondary standards that were run concurrently with unknowns are also provided in Data Set 1.

1.3 Expert knowledge identification of Old Crow tephra from major element composition

We used expert knowledge assessment (by B.J.L. Jensen) of the detrital shard dataset to identify Old Crow tephra, based on its distinct major element composition as gleaned

from thousands of analyses in the literature (e.g., Preece et al., 2011) and from its use as a routine secondary standard for EPMA glass analyses at University of Alberta. This first assessment of Old Crow tephra identification was confirmed by visual analysis of K_2O vs CaO (in weight percent; wt%) plots (main text Fig. 3). The compositional field of Old Crow tephra is particularly distinct for this pair of oxides; bivariate plots of other oxide pairs are not as useful because of compositional overlap between Old Crow tephra and other Yukon, Alaska, and Kamchatka tephra with a similar SiO_2 wt% range.

1.4 Classification and validation: a machine learning approach to identifying Old Crow tephra in the Site U1345 detrital shard population

We also used machine learning classification to independently identify shards of Old Crow tephra (OCt) from the Site U1345 detrital shard major element composition dataset. The classification approach closely follows Bolton et al. (2020), using an Artificial Neural Network and Random Forest (ANN and RF) ensemble.

We modified the Bolton et al. (2020) approach to include:

- Additional training data pre-processing to normalize non-OCt imbalances in tephra representativity,
- The addition of correlated noise to the non-OCt data to better simulate a wide range of potential glass compositions,
- Optimizing log-loss (instead of kappa) during tuning and employing a probability threshold to balance cross-validation prediction errors of commission and omission,
- Chlorine wt% as a predictand, in addition to the major oxides employed by Bolton et al. (2020).

The input training data include 1470 OCt analyses from reference samples previously identified and over 17,000 analyses on other Quaternary tephras from Alaska, Yukon, and Kamchatka. These data were drawn from published literature (Preece et al., 1999, 2011; Kaufman et al., 2001; Péwé et al., 2006; Jensen et al., 2008, 2011, 2013, 2016; Westgate et al., 2013; Davies et al., 2016) and the Tephrakam database (Portnyagin et al., 2020).

The training data pre-processing is as follows (Fig. S2). First, OCt analyses were separated from the incoming Alaska/Yukon data and held aside without further manipulation (except for centring and scaling, as stipulated by Bolton et al. 2020). Then, the remaining Alaska/Yukon data and Kamchatka data were joined and subjected to SMOTE (Synthetic Minority Over-sampling Technique) processing (Chawla et al., 2002). The SMOTE algorithm acts to systematically oversample under-represented classes in a dataset using a nearest neighbour-type approach, such that “new” data are randomly generated along the vectors between nearby neighbours while over-represented classes are simultaneously down-sampled. In this way, each tephra identified in the non-OCt dataset is adjusted to be similarly representative. Such a process was necessary due to the imbalances present in the dataset: some tephras,

such as VT and Chester Bluff (CB1), are very well characterized, with ~600 points each (and ten others represented by > 200 data points), whereas more than 250 other tephra in the dataset had 30 or fewer analyses each. In total, 402 unique non-OCt tephra are represented in the training data. Once SMOTE was completed, the dataset comprised 17,113 points, with each tephra represented by ~43 points each.

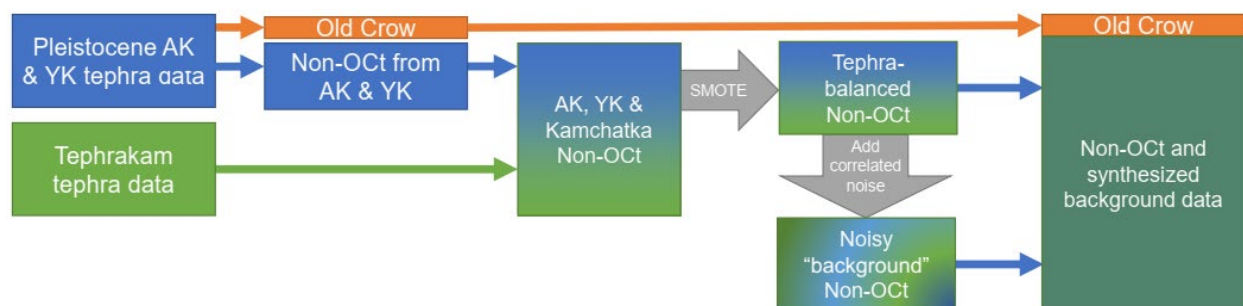


Fig. S2: Diagrammatic representation of training data processing workflow

However, our goal was not to identify distinct non-OCt tephra but to characterize the full diversity of compositions encompassed by the label “not Old Crow tephra”. As such, we supplemented our analyses and SMOTE-generated data with an equally-sized dataset synthesized by adding 150% correlated noise to the tephra-balanced non-OCt data. Such a noise addition process assumes noise should be normally distributed while maintaining the covariance structure of the original dataset (Brand, 2002). As a result, a wide range of potential compositions is generated, while the sums of major oxides remain at ~100%. To give an idea of the effect of noise addition, the mean SiO₂ of the tephra-balanced data was 71.73 weight-percent and ranged between 48.83 and 80.38. In comparison, the noise-added dataset had a similar mean (70.31) but ranged from 24.75 to 113.54. Such a difference in ranges highlights the strength of such a correlated noise structure. Without limiting the dataset to weight-percents between 0 and 100, not only is the full array of “reasonable” and expected glass compositions generated, but “impossible” (or at least improbable) ones are produced too, while still maintaining realistic comparisons between analytes. This also circumvents problematically skewing the synthetic geochemical data in an attempt to impose “closure”.

The two parts of the ensemble model were trained independently on the entire training set, comprised of (1) Old Crow analyses and (2) the combined non-OCt and synthesized background data. Tuning was conducted by varying model hyperparameters over a grid and bootstrap resampling the data, repeated 25 times for each hyperparameter setting. Hyperparameters were selected to minimize log-loss and, ideally, produce models with consistent probability profiles. In this case, the selected RF learner sampled three variables at each decision tree split, and the ANN model had 19 nodes in its hidden layer and used a decay value of 0.01778279. Although accuracy was not directly optimized, this routine still returned very high bootstrapped performance (ANN = 99.93%; RF = 99.95%).

Although the non-OCt tephras were balanced concerning their representativity within the non-OCt training data, a significant class imbalance remained between the “positive case” (OCt) and the “negative case” (non-OCt and background). The ratio between the two cases was about 1:24. We employed so-called threshold-moving to balance the sensitivity and specificity of the learners. By varying the probability decision threshold that defines the split between a positive and a negative case, we found the threshold wherein false positives and false negatives were most balanced in the bootstrapped dataset. This so-called “optimal” threshold is visualized as the point where the sensitivity and specificity curves intersect for a given model (Fig. S3). In this study, both the RF and ANN base-learners had optimal thresholds at 0.882. Thus, we used this value as the decision threshold for the mean ensemble that combined their predictions (Data Set 2).

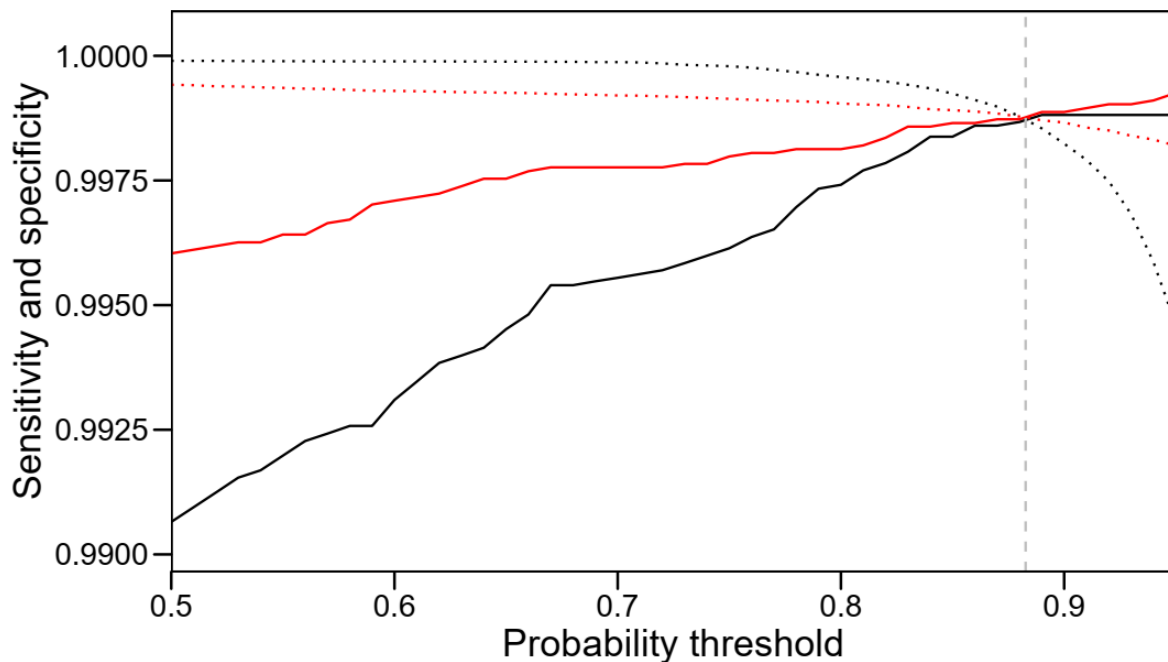


Fig. S3: Sensitivity and specificity plot for two component classification models evaluated over a range of probability thresholds. Dotted lines = sensitivity; solid lines = specificity; vertical dashed grey line = optimal threshold; black lines = RF; red lines = ANN

In addition to making predictions on the EPMA data collected for the present study, we also tested the OCt classifier ensemble on a different dataset of previously identified tephra to validate it. This test set contained analyses of OCt shards and Holocene tephras from AK, both of which were withheld from the training set. This test allows us to critically evaluate the sensitivity of the model both to detect and label Old Crow tephra shards not included in the training data and other non-OCt compositions. In this case, we evaluate the primary (i.e., non-detrital) tephras from the Eklutna Lake record in Alaska (Fortin et al., 2019; Bolton et al., 2020) and the secondary standard data for OCt

that were collected concurrently and published with this dataset. Evaluation of the OCT classifier ensemble on this test set, treating OCT as the “positive class”, reveals a sensitivity of 0.9695, a specificity of 1.0000, overall accuracy of 0.9956 (95% CI: 0.9887-0.9988), and a kappa value of 0.9819. When the four presumed false negative OCT points were scrutinized, they were found to be contaminated by microlites (i.e., they were mixed glass/mineral analyses). Excluding these contaminated points gives percent performance (accuracy = 1; 95% CI: 0.9959-1). This performance indicates that the OCT classifier is robust and generalizable, and reliably makes predictions on new data not included in its training dataset. Put simply, the validation test successfully identified all non-microlite-contaminated OCT shards as OCT, and did not identify any non-OCT shards as OCT.

Compared to the expert knowledge assessment (Section 1.3), the machine learning classifier applied to the Site U1345 detrital shard dataset identified the same shards as Old Crow. Similarly, the machine learning classifier did not identify any shards as Old Crow tephra that were not flagged as Old Crow tephra by expert knowledge assessment.

1.6 References

Asahi, H., Kender, S., Ikehara, M., Sakamoto, T., Takahashi, K., Ravelo, A.C., Alvarez, Zariqian, C.A., Khim, B.K., and Leng, M.J., 2016, Orbital-scale benthic foraminiferal oxygen isotope stratigraphy at the northern Bering Sea Slope Site U1343 (IODP Expedition 323) and its Pleistocene paleoceanographic significance: Deep-Sea Research II, v. 125-126, p. 66-83, doi:10.1016/j.dsr2.2014.01.004.

Blaauw, M., and Christen, A.J., 2011, Flexible paleoclimate age-depth models using an autoregressive gamma process: Bayesian Analysis, v. 6, p. 457-474, doi:10.1214/11-BA618.

Bolton, M.S.M., Jensen, B.J.L., Wallace, K., Praet, N., Fortin, D., Kaufman, D., and De Batist, M., 2020, Machine learning classifiers for attributing tephra to source volcanoes: an evaluation of methods for Alaska tephra: Journal of Quaternary Science, v. 35, p. 81–92, doi:10.1002/jqs.3170.

Burgess, S.D., Vazquez, J.A., Waythomas, C.F., and Wallace, K.L., 2021, U–Pb zircon eruption age of the Old Crow tephra and review of extant age constraints: Quaternary Geochronology, v. 66, 101168, doi:10.1016/j.quageo.2021.101168.

Buryak, S.D., Reyes, A.V., Jensen, B.J.L., Davies, J.H.F.L., Westgate, J.A., DuFrane, S.A., Luo, Y., Froese, D.G., and Pearson, D.G., in revision, Zircon U-Pb dates for key Pliocene-Pleistocene tephra beds in unglaciated Yukon and Alaska: accepted 9 June 2022 pending minor revision, Quaternary Geochronology [manuscript available for review purposes at www.ualberta.ca/~areyes/stuff/Buryak_manuscript.pdf]

Brand, R., 2002, Microdata protection through noise addition, in Domingo-Ferrer, J. ed., Inference Control in Statistical Databases: From Theory to Practice, Berlin, Heidelberg, Springer Berlin Heidelberg, p. 97–116, doi:10.1007/3-540-47804-3_8.

Chawla, N.V., Bowyer, K.W., Hall, L.O., and Kegelmeyer, W.P., 2002, SMOTE: Synthetic minority over-sampling technique: The Journal of Artificial Intelligence Research, v. 16, p. 321–357, doi:10.1613/jair.953.

Cook, M.S., Ravelo, A.C., Mix, A., Nesbitt, I.M., and Miller, N.V., 2017, Tracing subarctic Pacific water masses with benthic foraminiferal stable isotopes during the LGM and late Pleistocene: Deep-Sea Research II, v. 125-126, p. 84-95, doi:10.1016/j.dsr2.2016.02.006.

Davies, L.J., Jensen, B.J.L., Froese, D.G., and Wallace, K.L., 2016, Late Pleistocene and Holocene tephrostratigraphy of interior Alaska and Yukon: key beds and chronologies over the past 30,000 years: Quaternary Science Reviews, v. 146, p. 28–53, doi:10.1016/j.quascirev.2016.05.026.

Fortin, D., Praet, N., McKay, N.P., Kaufman, D.S., Jensen, B.J.L., Haeussler, P.J., Buchanan, C., and De Batist, M., 2019, New approach to assessing age uncertainties – the 2300-year varve chronology from Eklutna Lake, Alaska (USA): Quaternary Science Reviews, v. 203, p. 90–101, doi:10.1016/j.quascirev.2018.10.018.

Jensen, B.J.L., Evans, M.E., Froese, D.G., and Kravchinsky, V.A., 2016, 150,000 years of loess accumulation in central Alaska: Quaternary Science Reviews, v. 135, p. 1–23, doi:10.1016/j.quascirev.2016.01.001.

Jensen, B.J.L., Reyes, A.V., Froese, D.G., and Stone, D.B., 2013, The Palisades is a key reference site for the middle Pleistocene of eastern Beringia: new evidence from paleomagnetism and regional tephrostratigraphy: Quaternary Science Reviews, v. 63, p. 91–108, doi:10.1016/j.quascirev.2012.11.035.

Jensen, B.J.L., Preece, S.J., Lamothe, M., Pearce, N.J.G., Froese, D.G., Westgate, J.A., Schaefer, J., and Begét, J., 2011, The Variegated (VT) tephra: A new regional marker for middle to late Marine Isotope Stage 5 across Yukon and Alaska: Quaternary International, v. 246, p. 312–323, doi:10.1016/j.quaint.2011.06.028.

Jensen, B.J.L., Froese, D.G., Preece, S.J., Westgate, J.A., and Stachel, T., 2008, An extensive middle to late Pleistocene tephrochronologic record from east-central Alaska: Quaternary Science Reviews, v. 27, p. 411–427, doi:10.1016/j.quascirev.2007.10.010.

Kaufman, D.S., Manley, W.F., Wolfe, A.P., Hu, F.S., Preece, S.J., Westgate, J.A., and Forman, S.L., 2001, The last interglacial to glacial transition, Togiak Bay, southwestern Alaska: Quaternary Research, v. 55, p. 190–202, doi:10.1006/qres.2001.2214.

Keller, C.B., Schoene, B., Samperton, K.M., 2018, A stochastic sampling approach to zircon eruption age interpretation: *Geochemical Perspectives Letters*, v. 8, p. 31–35, doi:10.7185/geochemlet.1826.

Knudson, K.P., and Ravelo, A.C., Enhanced subarctic Pacific stratification and nutrient utilization during glacials over the last 1.2 Myr: *Geophysical Research Letters*, v. 42, p. 9870–9879, doi:10.1002/2015GL066317.

Kuehn, S.C., Froese, D.G., Shane, P.A.R., INTAV Intercomparison Participants, The INTAV intercomparison of electron-beam microanalysis of glass by tephrochronology laboratories: Results and recommendations: *Quaternary International*, v. 246, p. 19–47, doi:10.1016/j.quaint.2011.08.022.

Péwé, T.L., Westgate, J.A., Preece, S.J., Brown, P.M., and Leavitt, S.W., 2009, Late Pliocene Dawson Cut Forest Bed and new tephrochronological findings in the Gold Hill Loess, east-central Alaska: *Geological Society of America Bulletin*, v. 121, p. 294–320, doi:10.1130/b26323.1.

Portnyagin, M.V., Ponomareva, V.V., Zelenin, E.A., Bazanova, L.I., Pevzner, M.M., Plechova, A.A., Rogozin, A.N., and Garbe-Schönberg, D., 2020, TephraKam: geochemical database of glass compositions in tephra and welded tuffs from the Kamchatka volcanic arc (northwestern Pacific): *Earth System Science Data*, v. 12, p. 469–486, doi:10.5194/essd-12-469-2020.

Preece, S.J., Westgate, J.A., Froese, D.G., Pearce, N., and Perkins, W.T., 2011, A catalogue of late Cenozoic tephra beds in the Klondike goldfields and adjacent areas, Yukon Territory: *Canadian Journal of Earth Sciences*, v. 48, p. 1386–1418, doi:10.1139/e10-110.

Preece, S.J., Westgate, J.A., Stemper, B.A., and Péwé, T.L., 1999, Tephrochronology of late Cenozoic loess at Fairbanks, central Alaska: *Geological Society of America Bulletin*, v. 111, p. 71–90, doi:10.1130/0016-7606(1999)111<0071:TOLCLA>2.3.CO;2

R Core Team (2022). R: A language and environment for statistical computing. R Foundation for Statistical Computing, Vienna, Austria, <https://www.R-project.org>.

Sakata, S., 2018, A practical method for calculating the U-Pb age of Quaternary zircon: Correction for common Pb and initial disequilibria: *Geochemical Journal*, v. 52, p. 281–286, doi:10.2343/geochemj.2.0508.

Springer, A.M., McRoy, C.P., and Flint, M.V., 1996, The Bering Sea Green Belt: shelf-edge processes and ecosystem production: *Fisheries Oceanography*, v. 5, p. 205–223, doi:10.1111/j.1365-2419.1996.tb00118.x.

Westgate, J.A., William Pearce, G., Preece, S.J., Schweger, C.E., Morlan, R.E., Pearce, N.J.G., and William Perkins, T., 2013, Tephrochronology, magnetostratigraphy and

mammalian faunas of Middle and Early Pleistocene sediments at two sites on the Old Crow River, northern Yukon Territory, Canada: *Quaternary Research*, v. 79, p. 75–85, doi:10.1016/j.yqres.2012.09.003.

Worne, S., Kender, S., Swann, G.A., Leng, M.J., Ravelo, A.C., 2019, Coupled climate and subarctic Pacific nutrient upwelling over the last 850,000 years: *Earth and Planetary Science Letters*, v. 522, p. 87-97, doi:10.1016/j.epsl.2019.06.028.

Table S1. Revised age-depth model for Site U1345, updated from Cook et al., 2016.

	LR04 Stack	U1345
	Age (ka)	Depth (m CCSF-A)
Core top	0	0.0 ± 1.0
MIS 2/1	14	6.0 ± 0.5
MIS 5/4	71	23.6 ± 1.0
MIS 6/5*	130	35.2 ± 0.2
MIS 7/6	191	47.8 ± 1.0
MIS 7 $\delta^{18}\text{O}$ max**	223	57.7 ± 0.2
MIS 8/7	243	68.7 ± 1.0
MIS 9/8	300	87.0 ± 2.0

* revised uncertainty based on correlation of abrupt $\delta^{15}\text{N}$ transition

**new tie point

Table S2. Summary of Site U1345 detrital glass samples (Cook et al., 2016; Expedition 323 Scientists, 2011)

University of Alberta accession number	Depth (m CCSF-A)	Age (ka) ^a	±age (ka) ^b	Benthic $\delta^{18}\text{O}$ (VPDB) ^c	U1345 hole-core-section	shards analyzed ^d	Old Crow tephra shards	Old Crow tephra shard concentration (%)	Sedimentology ^e	Bioturbation ^e
UA 3744	6.26	14.7	3.6	4.54	U1345D-1H-4	50	4	8.0	sandy silt	absent
UA 3745	23.16	69.6	5.1	4.37	U1345C-3H-4	50	2	4.0	silt	slight
UA 3746	28.09	93.8	9.2	4.20	U1345A-4H-3	49	2	4.1	silt	slight
UA 3747	32.25	115.0	8.1	4.25	U1345A-4H-6	50	7	14.0	silt	slight
UA 3748	33.07	119.2	7.2	4.16	U1345D-4H-1	50	3	6.0	silt	slight
UA 3749	36.07	134.2	5.6	4.60	U1345D-4H-3	101	9	8.9	sandy silt	slight
UA 3750	37.59	141.6	7.5	4.49	U1345D-4H-4	101	50	49.5	silty clay	slight
UA 3833	38.35	145.3	8.1	4.45	U1345D-4H-4	101	63	62.4	silty clay	slight
UA 3868	38.50	146.0	8.2	4.08	U1345A-5H-3	92	45	48.9	diatom sandy silt	absent
UA 3834	38.87	147.8	8.5	4.31	U1345A-5H-4	50	30	60.0	diatom sandy silt	absent
UA 3835	40.02	153.3	9.1	4.20	U1345A-5H-4	50	22	44.0	diatom sandy silt	absent
UA 3836	40.74	156.8	9.2	4.37	U1345A-5H-5	50	20	40.0	diatom sandy silt	absent
UA 3861	41.34	159.7	9.2	4.51	U1345A-5H-5	50	0	0.0	diatom sandy silt	absent
UA 3862	41.94	162.6	9.3	4.36	U1345A-5H-6	50	0	0.0	diatom sandy silt	absent
UA 3863	42.34	164.6	9.3	4.56	U1345A-5H-6	48	1	2.1	laminated diatom sandy silt	absent
UA 3751	42.98	167.7	9.1	4.36	U1345C-5H-4	99	0	0.0	silt	absent
UA 3837	43.10	168.3	9.1	4.26	U1345C-5H-4	100	0	0.0	silt	absent
UA 3864	44.26	173.9	8.7	4.29	U1345C-5H-5	47	0	0.0	laminated clayey sand	absent
UA 3865	45.78	181.2	7.3	4.25	U1345C-5H-6	50	0	0.0	clayey sand	absent
UA 3866	47.39	189.0	5.0	4.26	U1345A-6H-2	50	0	0.0	sandy silt	slight
UA 3867	49.61	196.9	5.6	4.06	U1345A-6H-3	97	0	0.0	sandy silt	slight
UA 3752	51.13	201.8	5.9	3.84	U1345A-6H-4	100	0	0.0	sandy silt	slight
UA 3838	52.61	206.6	5.9	3.95	U1345A-6H-5	100	0	0.0	sandy silt	slight
UA 3753	53.66	210.0	5.7	3.88	U1345C-6H-4	100	0	0.0	silt	slight
UA 3754	56.66	219.8	4.2	4.21	U1345C-6H-6	49	0	0.0	silty clay	slight
UA 3755	66.03	238.2	4.1	3.68	U1345C-7H-5	49	0	0.0	clayey silt	moderate
UA 3756	73.06	256.6	6.4	4.49	U1345C-8H-3	52	0	0.0	clayey silt	moderate
UA 3757	74.22	260.2	6.9	4.50	U1345C-8H-4	51	0	0.0	clayey silt	moderate

^aupdated from Cook et al. (2016); details in Appendix DR1

^b2sigma uncertainty from BACON (Blaauw and Christen, 2011) age model; details in Appendix DR1

^cfrom Cook et al. (2016)

^dnumber of shards excludes analyses with phenocrysts/microlites

^efrom Expedition 323 Scientists (2011)